# In-Situ Thermochemical Shock-Induced Stress at the Metal/Oxide Interface Enhances Reactivity of Aluminum Nanoparticles

Prithwish Biswas, Feiyu Xu, Pankaj Ghildiyal, and Michael R. Zachariah*

Cite This: ACS Appl. Mater. Interfaces 2022, 14, 26782−26790   Read Online

ACCESS | Metrics & More | Article Recommendations | SI Supporting Information

**ABSTRACT:** Although aluminum (Al) nanoparticles have been widely explored as fuels in energetic applications, researchers are still exploring approaches for tuning their energy release profile via microstructural alteration. In this study, we show that a nanocomposite (∼70 nm) of a metal ammine complex, such as tetraamine copper nitrate $(Cu(NH_3)_4(NO_3)_2/TACN)$, coated Al nanoparticles containing only 10 wt. % TACN, demonstrates a ∼200 K lower reaction initiation temperature coupled with an order of magnitude enhancement in the reaction rate. Through time/temperature-resolved mass spectrometry and ignition onset measurements at high heating rates, we show that the ignition occurs due to a condensed phase reaction between Al and copper oxide (CuO) crystallized on TACN decomposition. TEM and XRD analyses on the nanoparticles at an intermediate stage show that the rapid heat release from TACN decomposition in-situ enhances the strain on the Al core with induction of nonuniformities in the thickness of its $AlO_x$ shell. The thinner region of the nonuniform shell enables rapid mass transfer of Al ions to the crystallized CuO, enabling their condensed phase ignition. Hence, the thermochemical shock from TACN coating induces stresses at the $Al/AlO_x$ interface, which effectively switches the usual gas phase $O_2$ diffusion-limited ignition process of Al nanoparticles to become condensed phase Al ion transfer controlled, thereby enhancing their reactivity.

**KEYWORDS:** *metal, nanoparticles, metal oxides, nanothermite, energetic materials, interfaces, lattice strain, redox reactions*
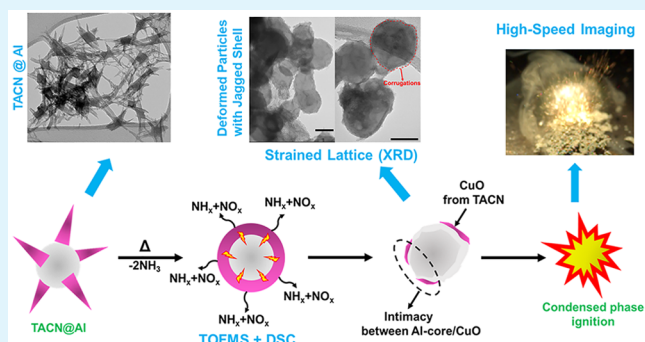
## 1. INTRODUCTION

Among the nanometallic fuels used in energetic materials for propulsion and pyrotechnics,[1−3] Aluminum (Al) is the most commonly employed fuel due to its high gravimetric (∼32 kJ/g) and volumetric combustion enthalpy (∼86 kJ/cm³).[4−12] Extensive efforts have been employed in modulating the energy release profile of Al nanoparticles in fuel/oxidizer composites by altering the ionic conductivity of oxidizers,[13−15] oxidizer morphology,[16−18] and utilization of additives[19−21] to improve reactivity.

Several studies have focused on improving the reactivity of Al nanoparticles by their microstructural alteration through induction of thermomechanical stresses.[22−32] The core of the Al nanoparticles nominally exists under tensile stress at room temperature, which attains a zero-strain state when heated to ∼673 K.[33] It has been observed that preannealing of Al nanoparticles at around ∼673 K for several minutes followed by fast quenching induces dilatational lattice strain on the core, which appears to enhance Al transport through the shell.[22−32] Additionally, an investigation on aging behavior of nanothermite composites of Al with oxidizers such as CuO, $Fe_2O_3$, and $Co_3O_4$, by annealing of the mixtures at ∼473 K for 15 days, showed that the alumina shell became nonuniform in

thickness.[34] The nonuniformity in the thickness of the shell led to a higher mass transport rate of Al through the thinner regions, resulting in an unexpectedly high reactivity of the annealed nanothermite composites.

In this regard, Werner-type metal ammine complexes[35−39] such as tetraamine copper nitrate $(Cu(NH_3)_4(NO_3)_2/TACN)$ can be used with Al nanoparticles for two potential benefits. First, it can act as a reactive gas generator by exothermically $(\Delta H \sim -644 \text{ kJ/mol})$[37] decomposing to $NH_x$ and $NO_x$ gases, leaving residual CuO to participate in a redox reaction with Al. This has important implications with respect to Al combustion as the phase transformation of Al during high-temperature oxidation processes together with the high mobility of Al ions through its oxide shell results in rapid sintering and agglomeration of Al nanoparticles, thereby impeding the progress of the energetic reaction.[9,33,40−43] In-situ gas
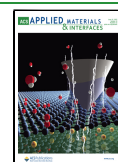
generation through polymeric additives has been effective in mitigating this problem, as gas generation during high-temperature decomposition of these polymers reduces sintering and agglomeration by pushing particles away from each other.[44] Therefore, TACN can be potentially used for in-situ gas generation for mitigating similar challenges. Secondarily, as prestressing has been shown to improve the reactivity of Al, the rapid energy released during TACN decomposition can be potentially employed to shock-heat and induce strain in the Al nanoparticles. Hence, this approach may be able to mitigate the preprocessing steps associated with the annealing.[22−32] Previous explorations have shown that the use of super-micrometer TACN particles as gas generating additives can significantly improve the reactivity of Al/CuO composites.[45−47] However, the application of nanoscale TACN for in-situ stress induction in Al nanoparticles has not been explored.

In this study, we have synthesized ∼70 nm particles of TACN-coated Al (TACN@Al) by a heterogeneous crystallization method. The synthesis of bare TACN crystals in the absence of Al nanoparticles as seed led to the formation of ∼4 $\mu$m TACN particles. Using in-situ T-jump ignition, T-jump time-of-flight mass spectrometry (T-jump TOFMS), and TGA/DSC analysis, we show that the heat released on decomposition of TACN in TACN@Al into $NH_x$ and $NO_x$ species is absorbed by Al nanoparticles, resulting in their early oxidation and condensed phase ignition. Through XRD and TEM, we have shown that the released heat collectively deforms the Al particles, enhances strain on the Al core, and induces nonuniformity in the thickness of the alumina shell. The thinner regions of the nonuniform shell having shorter diffusion length enable the Al ions to diffuse across the shell and initiate a condensed phase reaction with the oxidizer, thereby lowering the oxidation and ignition onsets. Such an effect was not observed in the case of physically mixed Al with micrometer TACN, as the processes of TACN decomposition and Al oxidation occurred independently.

## 2. EXPERIMENTAL SECTION

**2.1. Materials.** Aluminum nanoparticles (ALEX) with a mean size of ∼50 nm and having an Al content of ∼67 mass % was procured from Argonide Corp. The copper nitrate trihydrate ($Cu(NO_3)_2 \cdot 3H_2O$) salt was obtained from Sigma-Aldrich. The 30% $NH_4OH$ and ethanol were procured from Fisher Scientific. The CuO nanoparticles (∼50 nm) were obtained from US Research Nanomaterials.

**2.2. Synthesis of TACN-Coated Al Composites.** Previous studies have synthesized TACN crystals by a precipitation reaction between dissolved $Cu(NO_3)_2$ and $NH_4OH$.[45] To make TACN-coated Al composites (TACN@Al), we prepared various strengths (0.2, 0.4, 0.8, and 1.6 mM) of copper nitrate trihydrate ($Cu(NO_3)_2 \cdot 3H_2O$) solutions in ethanol. Equal amounts of Al nanoparticles (∼50 nm) were ultrasonically dispersed in all of the $Cu(NO_3)_2$ solutions, such that the mass concentration of Al in each solution is 0.5 mg/mL. The concentration of $Cu(NO_3)_2$ was varied with the goal to make different TACN@Al composites with TACN content varying between 5 and 20 mass %. The $Cu(NO_3)_2$ solutions with dispersed Al nanoparticles were magnetically stirred for ∼10 min. Then 30% $NH_4OH$ was added dropwise to each of the $Cu(NO_3)_2$ solutions with dispersed Al nanoparticles under vigorous magnetic stirring. As 4 mol of $NH_3$ needs to be inserted into 1 mol of $Cu(NO_3)_2$ to make TACN, the total amount of $NH_4OH$ added to each solution was varied to ensure that the final $NH_4OH$ concentration is 4 times the concentration of dissolved $Cu(NO_3)_2$. After $NH_4OH$ addition, each solution was kept under magnetic stirring for ∼1 h. Then each solution was centrifuged and washed (10000 rpm, 10 min) with blank solvents two times. The washed powders were dried overnight in a vacuum oven at room temperature. For the synthesis of the bare TACN crystals, we started with a 0.8 mM $Cu(NO_3)_2 \cdot 3H_2O$ solution and followed the exact same procedure, except for the addition of Al nanoparticles.

**2.3. Ex-Situ Characterizations on Composition and Material Properties.** Particle sizes and morphologies of TACN and TACN@Al were characterized by an FEI NNS450 scanning electron microscope (SEM) and an FEI Tecnail 12 transmission electron microscope (TEM). X-ray diffraction (XRD), performed by using PANalytical EMPYREAN (Cu K$\alpha$ source, $\lambda$ = 1.54 Å), was used to characterize the composition, lattice strain, and crystallite size of the TACN@Al crystals. Thermogravimetric analysis (TGA) and differential scanning calorimetry (DSC) performed by using an SDT-Q600 (TA Instruments) were used to characterize the decomposition steps of TACN and the oxidation onset of Al, at a heating rate of 10 K/min. The TACN content of each sample was also identified through TGA.

**2.4. In-Situ Time- and Temperature-Resolved Characterization on Ignition and Combustion.** Temperature jump time-of-flight mass spectrometry (T-jump TOFMS) was used for in-situ time- and temperature-resolved identification of the gas phase species released during the preignition and combustion reactions. Details about the mass spectrometer can be found in several of our previous publications.[3,48,49] For this measurement, a thin Pt wire (∼75 $\mu$m) is used as the sample holder, on which thin layers of solid nanopowder samples are coated by drop-casting through micropipets. During the measurement, the Pt wire is resistively heated to ∼1500 K by applying a voltage pulse of width ∼3 ms, which leads to an average heating rate of ∼$10^5$ K/s. The thin coating of the sample ensures that the sample is at the same instantaneous temperature as that of the wire and that it is uniformly heated at the same heating rate. Through a probe, the current across the wire is monitored at every 0.1 ms, and the Callendar−Van Dusen equation is used to estimate the instantaneous wire temperature at every 0.1 ms over the 3 ms pulse. The gas phase species released on thermal activation of the reactions are sampled and identified over 10 ms at an interval of 0.1 ms by the time-of-flight mass spectrometric process. This measurement is performed under a high vacuum of ∼$10^{-10}$ atm.

The ignition temperature of each sample was measured by using a similar temperature jump process (T-jump ignition). The sample holder and the sample delivery, heating, and temperature estimation methods of this measurement are exactly the same as those of T-jump TOFMS. However, instead of a vacuum, this measurement is performed by inserting the sample holder into a specialized chamber equipped with several ports for flowing gases and applying a vacuum along with a pressure gauge and a quartz glass wall for high-speed imaging of the ignition event, which is filled with Ar at ∼1 atm. A high-speed camera (Vision Research Phantom V12.1) is used to track the delay time of the ignition event with approximately microsecond resolution. The temperature of the wire at this time is estimated to be the ignition temperature. More details about this measurement can be found in our previous papers.[3,50] The T-jump ignition and TOFMS characterizations cannot be performed on the supermicron bare TACN crystals and PM-TACN/Al as those particle sizes are comparable to the thickness of the Pt wire sample holder, which leads to nonuniform coatings resulting in inconsistencies in the temperature measurement.

Constant-volume combustion cell measurements were performed to characterize the pressurization rate and burn time of the self-propagating combustion reaction. A charge of 25 mg is used for every measurement in the ∼20 cm$^3$ cell. The powdered sample is ignited at the center by the tip of a resistively heated nichrome wire which touches only the surface sample. During the progress of the reaction, the time-dependent pressure and optical signal is monitored by a high-frequency pressure transducer (PCB electronics) and a photo-multiplier tube (Hamamatsu), respectively. More details about the measurement can be found elsewhere.[3,19]
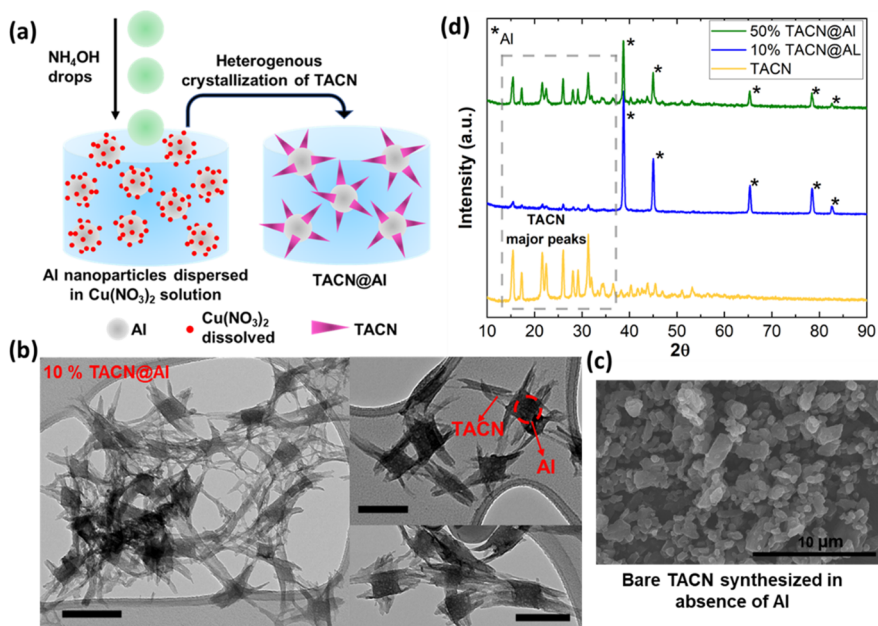
**Figure 1.** (a) Schematic showing the preparation of TACN@Al nanocomposite by heterogeneous crystallization method. (b) Representative TEM images of synthesized TACN@Al composites showing the growth of needlelike TACN crystals on Al particles (scale bar: 100 nm). (c) SEM images of supermicron TACN crystals synthesized by homogeneous crystallization method in the absence of Al seeds. (d) XRD spectra confirm the presence of TACN and Al in the nanocomposites, also clearly showing an increase in the intensity of TACN peaks relative to that of Al with increase in TACN content.
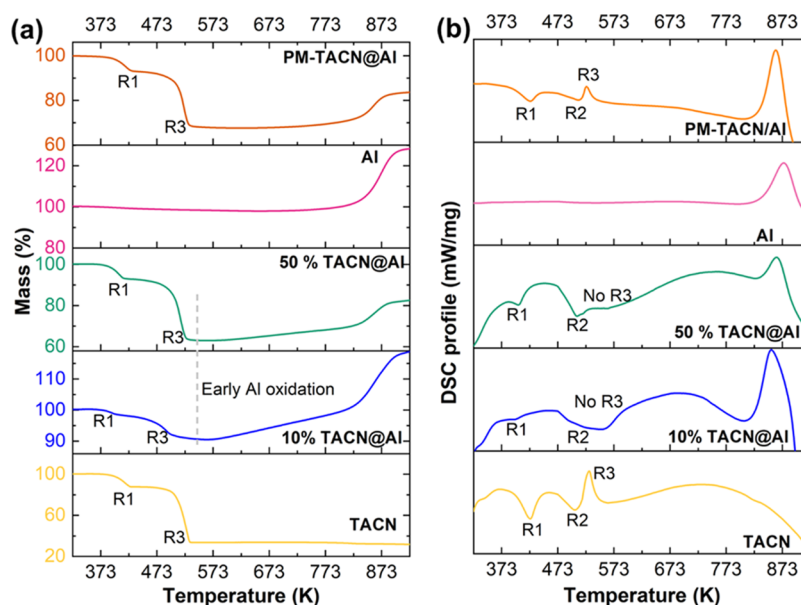


**Figure 2.** (a) TGA shows the decomposition of TACN in bare TACN, TACN@Al, and PM-TACN/Al occurs in two mass loss steps; however, the Al in TACN@Al shows an early oxidation onset initiating exactly after TACN decomposition. (b) DSC shows the decomposition of TACN in bare TACN, and PM-TACN/Al has two endothermic peaks (R1 and R2) and one exothermic peak (R3), whereas the exothermic peak disappears in the case of TACN@Al.

## 3. RESULTS AND DISCUSSION

### 3.1. Synthesis of TACN-Coated Al Nanocomposites.
TACN-coated Al nanoparticles are synthesized by a heterogeneous crystallization (Figure 1a) process as described in section 2.1. Representative TEM images (Figure 1b) of 10 mass % TACN@Al clearly show the growth of needlelike TACN crystals on the surface of Al particles. The mass percentages of TACN in the TACN@Al composites have been estimated through TGA as presented in the next section

(section 3.2). By varying the $Cu(NO_3)_2 \cdot 3H_2O$ precursor concentration relative to Al nanoparticle concentration (5−50%), we have synthesized TACN@Al composites containing various mass fractions of TACN. In the final composite, different initial precursor concentrations of 0.2, 0.4, 0.8, and 1.6 mM resulted in a TACN content of 4, 12, 21, and 48 mass %, respectively, as listed in Table S1 (Supporting Information). For the sake of simplicity, we have designated the TACN@Al composites with TACN contents of 4, 12, 21, and 48% as 5%
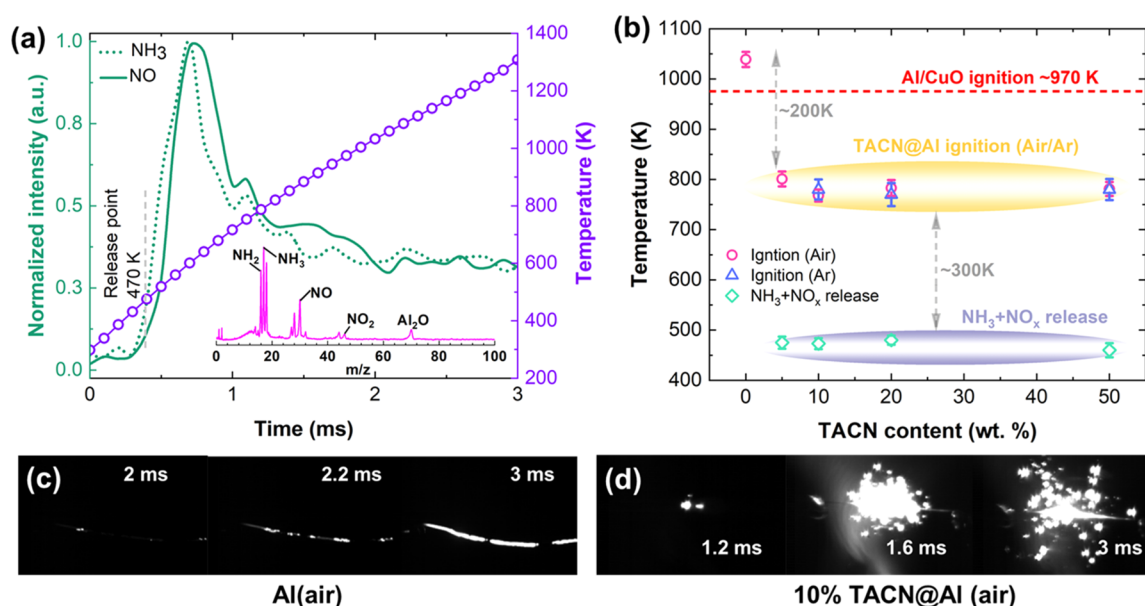
**Figure 3.** (a) T-jump TOFMS release profiles of $NH_3$ and NO species from 10% TACN@Al show that TACN decomposes at ~470 K at high heating rates (~$10^5$ K/s). The inset containing time-averaged mass spectrum of 10% TACN@Al shows the release of different $NH_x$ and $NO_x$ species. (b) Ignition temperatures of Al(air), Al/CuO, and TACN@Al composites with different TACN contents in Air and Ar show that all TACN@Al composites ignite at an ~200 K lower temperature. The ignition of 10% TACN@Al (d) with a small oxidizer content is unexpectedly more violent than that of Al in air (c).

TACN@Al, 10% TACN@Al, 20% TACN@Al, and 50% TACN@Al, respectively, in the rest of the article.

Dropwise addition of $NH_4OH$ to Al nanoparticles dispersed in $Cu(NO_3)_2 \cdot 3H_2O$ results in the heterogeneous nucleation and growth of TACN crystals, leading to the formation of core–shell TACN@Al (Figure 1a). Dropwise addition maintains a low concentration of $NH_4OH$ in the solution, thereby limiting homogeneous nucleation of TACN and restricting the size of TACN@Al to ~70 nm (Figure 1b and Figure S1a). For the purpose of preparing physically mixed Al/TACN control samples, bare TACN has been synthesized by precipitation in the absence of Al nanoparticles, keeping the rest of the procedure same (section 2.1). SEM micrographs (Figure 1c) of bare TACN show the formation of ~4 $\mu$m crystals (Figure S2b). Larger crystal sizes maybe attributed to slower homogeneous nucleation process. Figure 1d representing the XRD spectra of bare TACN, 10% TACN@Al, and 50% TACN@Al shows a clear variation between the relative peak intensities of Al and TACN, confirming the presence of different concentrations of TACN in different formulations of the composite.

### 3.2. Influence of the Thermochemical Decomposition of TACN on Al Oxidation under Slow Heating Rates.
Previous studies[35,45] have shown that the thermochemical decomposition of TACN/$Cu(NH_3)_4(NO_3)_2$ occurs in the following three major steps:
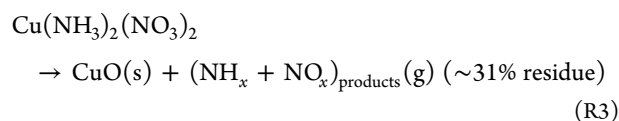
(i) endothermic release of 2 mol of $NH_3$ attached as a ligand to form $Cu(NH_3)_2(NO_3)_2$:

$$Cu(NH_3)_4(NO_3)_2 \rightarrow Cu(NH_3)_2(NO_3)_2(s) + 2NH_3(g)$$

$$(\sim 87\% \text{ residue}) \tag{R1}$$
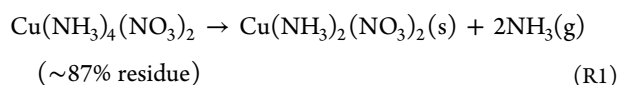
(ii) solid to liquid phase transformation of $Cu(NH_3)_2(NO_3)_2$:

$$Cu(NH_3)_2(NO_3)_2(s) \rightarrow Cu(NH_3)_2(NO_3)_2(l) \tag{R2}$$
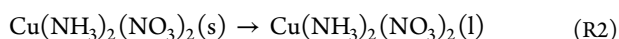
(iii) simultaneous exothermic formation of CuO and $NH_x$ + $NO_x$ species:

$$Cu(NH_3)_2(NO_3)_2$$
$$\rightarrow CuO(s) + (NH_x + NO_x)_{products}(g) \ (\sim 31\% \text{ residue}) \tag{R3}$$

We also observed all of the three aforementioned steps during the TGA/DSC characterization of bare TACN in air. The TGA curve of bare TACN (Figure 2a) shows two mass loss steps terminating at ~423 K (~87% residue) and ~533 K (~32% residue) corresponding to the chemical reactions presented in eqs R1 and R3, respectively. The simultaneous DSC profile of bare TACN obtained during the same measurement shows two endotherms at ~423 and ~493 K corresponding to eqs R1 and R2, respectively, followed by an exotherm associated with the second mass loss step corresponding to eq R3.

It is well-known that the oxidation onset of Al nanoparticles in air (~833 K) at low heating rates is governed by the formation of voids due to the crystallization of the native $Al_2O_3$ shell.[4] TGA/DSC on bare Al nanoparticles and physically mixed bare-Al/bare-TACN particles (PM-Al/TACN) shows that Al nanoparticles in PM-Al/TACN have the same oxidation onset (~833 K) as that of bare Al nanoparticles (Figure 2a,b). The TGA profile (Figure 2a) of PM-Al/TACN clearly shows the two-stage mass loss (eqs R1 and R3) during thermolysis of TACN and the mass gain on oxidation of Al occur independently, with the former phenomenon terminating at ~533 K and the latter reaction initiating at ~833 K. The DSC profile (Figure 2b) of PM-Al/TACN shows all the three peaks corresponding to eqs R1–R3 similar to that of bare TACN with the Al oxidation exothermic peak arising at ~833 K, also confirming that the TACN decomposition and Al oxidation occur separately.
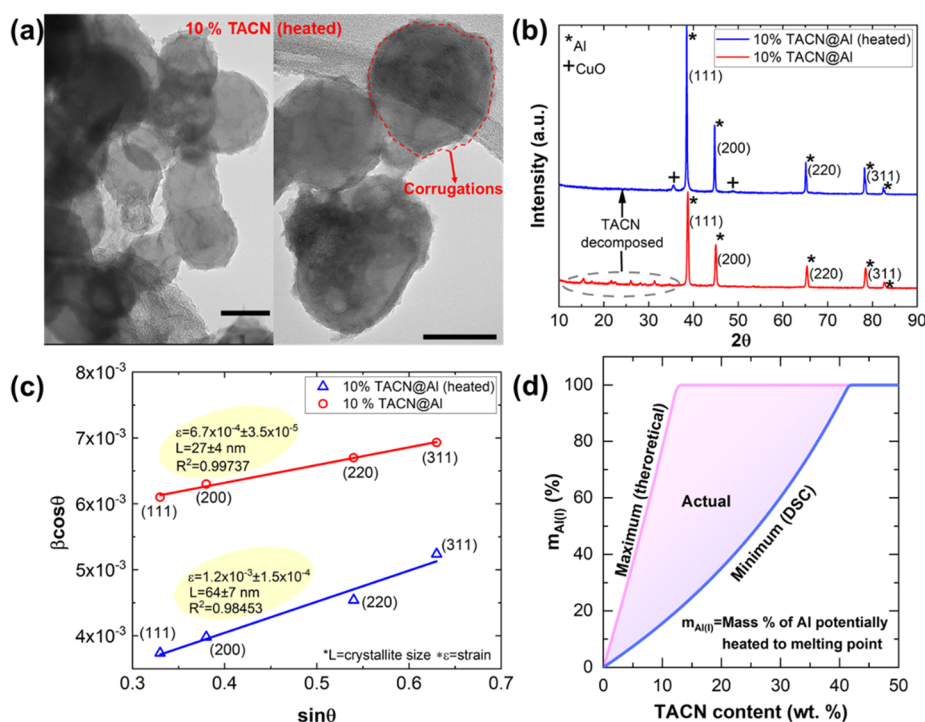
**Figure 4.** (a) TEM images of heated 10% TACN@Al show that Al particles deform and their shells become corrugated, post TACN decomposition (∼523 K) (scale bar: 100 nm). (b) XRD of the same particles show confirm that the TACN peaks have disappeared on heating and the heated particle only contains Al and CuO. (c) Williamson−Hall analysis of the XRD peaks show that he heated Al core in the heated particles possesses higher strain and crystallite size. (d) Estimated maximum and minimum mass percentages of Al that can be potentially melted by considering maximum (theoretical) and minimum (DSC) heat release from TACN, respectively.

However, in the case of the TACN-coated Al composites, both 10% TACN@Al and 50% TACN@Al, a gradual mass gain is observed right after the termination of the TACN decomposition at ∼533 K (Figure 2a). Additionally, only the two endothermic peaks corresponding to chemical equations (R1) and (R2) are observed in the DSC of both of these samples (Figure 2b), whereas the exothermic peak that is observed in the case of bare TACN due to the reaction in eq R3 is absent. Instead, a gradually rising exotherm is observed post ∼533 K concomitant with the gradual mass gain in TGA at the same temperature. The gradual mass gain and heat release initiating at ∼533 K are most likely due to the oxidation of Al, indicating that the Al in the preassembled TACN@Al samples have incurred an early oxidation onset. The absence of the exothermic peak corresponding to eq R3 implies that the heat release associated with this step has been absorbed by some parallel occurring endothermic process that is possibly contributing to the early oxidation of Al. Therefore, it is evident that the decomposition and energy release profile of the nanoscale TACN@Al composite differs significantly from that of both supermicrometer PM-TACN/Al formulation and bare Al, the underlying mechanism of which is investigated in the subsequent sections.

**3.3. Ignition and Combustion Reaction of TACN@Al at High Heating Rates.** In-situ temperature-resolved time-of-flight mass spectrometry (T-jump TOFMS) is used to probe the reaction mechanism during the ignition and combustion of TACN@Al, on activating at a high heating rate of ∼$10^5$ K/s. The inset of Figure 3a presenting the T-jump TOFMS time-averaged spectra of 10% TACN@Al shows the release of gaseous $NH_3$ and $NO_x$ species such as $N_2O$, $NO$, and $NO_2$. Upon comparison of the temporal intensity and temperature

profiles of these species (Figure 3a), their release temperature has been estimated to be ∼470 K. T-jump TOFMS spectra of all other TACN@Al composites also show the release of these species regardless of the TACN content (Figure S3). The $NO_x$ species are generated either from the decomposition of the $NO_3$ group or from the reaction between $NH_3$ and $NO_x$ groups, with CuO being the residual solid-state product as described in section 3.2. This indicates that the decomposition of TACN at high heating rates also occurs through the reactions presented in eqs R1−R3. Figure 3b shows that the release of all the gaseous species occurs around ∼470 K, for all TACN@Al composites, regardless of TACN content. The single step release of these gaseous species, in contrast to the two-stage TGA mass loss, can be attributed to the faster reaction kinetics at high heating rates in T-jump TOFMS, which makes it difficult to resolve multiple reaction steps involved.

T-jump ignition measurements performed in Air and Ar environments (∼1 atm) reveal that all the TACN@Al composites ignite at ∼770 K (Figure 3b). This ignition temperature is much lower compared to the ignition temperature of Al in air (by ∼270 K) and Al/CuO (by ∼200 K) as shown in Figure 3b. The snapshots from the high-speed imaging of the ignition events of bare Al and 10% TACN@Al in air are shown in Figures 3c and 3d, respectively. These images clearly show that the ignition event of bare Al is very mild with no particle ejections from the wire, indicating that the ignition event is not associated with intense gaseous expansion due to low energy release during the oxidation process. In contrast, the ignition event of 10% TACN@Al is associated with intense gas generation and expansion causing particle ejections, leading to a brighter and larger flame.

**Table 1. Comparison of Microstructural Evolution of Al Nanoparticles under Thermomechanical Stresses**

| reference | material | treatment | finding |
|---|---|---|---|
| Wu et al.[34] | Al/CuO-nanothermite | annealing (473 K, 15 days) | jagging of shell; enhanced mass transfer; enhanced reactivity |
| Jacob et al.[28] | Al nanoparticle | annealing (573 K, 15 min) | enhanced strain on Al core softens shell; no morphology change; enhanced reactivity |
| Firmansyah et al.[33] | Al nanoparticle | in-situ heating (10 K/min; ~$10^5$ K/s) | existing tensile strain on Al core at ~298 K; no morphology changes until ~873 K; swelling of shell on interstitial diffusion of Al ions |
| current study | TACN@Al | in-situ heating (10 K/min; ~$10^5$ K/s) | jagging of shell leading to lower oxidation and ignition onset |

Representative snapshots of the flames of different TACN@Al obtained during the T-jump ignition measurements can be found in Figure S4. Combustion cell measurements obtained with TACN@Al samples with different compositions of TACN, physically mixed with nano-CuO in stoichiometric amounts, show that 10% TACN@Al has the highest peak pressure (~2×), pressurization rate (~10×), and the shortest burn time (~50 ms less) among all TACN@Al samples (Figure S5). The reactivity of these composites initially increases with the increase in TACN content up to ~10% due to hot gas generation, and then it decreases with further increase in TACN content, as TACN with high molar mass reduces the gravimetric energy density of the TACN@Al composites. Although the trend of the measured pressurization rates is qualitatively similar to that of the observations made by Wu et al.,[45] an order of magnitude enhancement in pressurization rates has not been observed for physically mixed micrometer-TACN, Al, and CuO. An ~200 K lowering of ignition temperature, along with an order of magnitude enhancement in reactivity, on application of only 10 mass % of coating is unexpected.

As most of the $NO_x$ species are released at a lower temperature (~470 K), much earlier than the ignition event (~770 K), the possibility of Al/$NO_x$ being the source of ignition can be eliminated. Moreover, the higher ignition temperature of Al in air (~1050 K) and the similarity of the ignition temperature of TACN@Al composites in air and argon environments imply that the Al is not reacting with atmospheric oxygen prior to ~770 K. This implies that the ignition is possibly initiated by the reaction between Al and the condensed CuO formed after decomposition of TACN. Usually, physically mixed Al/CuO nanothermites ignite at 993 K, post $O_2$ release from CuO (~930 K) (Figures S6 and S7),[51] due to the heterogeneous reaction between gas phase $O_2$ with condensed Al. It is still uncertain why the TACN@Al composite initiates primarily in the condensed phase and ignites at an ~200 K lower temperature than Al/CuO, prior to the release of $O_2$ from CuO. The heat released during the TACN decomposition (R3) may have some contribution to the transition from gas phase initiation to condensed phase initiation, as it has been already observed in section 3.2 that the exothermic peak associated with this reaction during bare TACN decomposition disappears during the reaction of TACN@Al, indicating the released heat might be absorbed in activating some parallel occurring interactions. This uncertainty has been addressed with the depiction of the underlying reaction mechanisms in the subsequent sections.

**3.4. Intermediate Product Analysis Revealing In-Situ Stress Induction in Al Core.** To characterize the morphology and composition of the intermediate state of the Al particles post TACN decomposition by using ex-situ TEM/XRD, we heated the 10% TACN@Al particles, to the decomposition termination temperature of TACN (~533 K)

using the same TGA/DSC apparatus and cooled them under ambient conditions. XRD spectra (Figure 4b) of the heated 10% TACN@Al clearly show that the diffraction peaks belonging to TACN have disappeared, and the heated intermediate state only contains peaks of Al and CuO. TEM images of the heated 10% TACN@Al particles show nonspherical and deformed Al particles with corrugations near the surface (Figure 4a). Similar Al particles with rough surfaces have been also observed by Wu et al.[34] when they thermally annealed/aged a nanothermite mixture of Al/CuO at ~473 K for 15 days. They observed that the thickness of the alumina shell became nonuniform on annealing because of thermally induced stresses causing it to become jagged and claimed that the faster outward diffusion of Al through the thinner regions of the shell enhanced the reactivity of the annealed Al/CuO mixture. Independently, several other studies[22−32] have shown that annealing (473−573 K) of Al nano-/microparticles with native oxide shells enhances the lattice strain on the Al core, thereby reducing the hardness of the particles leading to their higher reactivity. However, the jagging of the shell in the current scenario might be due to a combination of several different factors, as systematically explained later.

Through a combination of in-situ XRD and TEM characterizations, Firmansyah et al.[33] have shown that the cores of Al nanoparticles are already under tensile stress at room temperature. We performed the Williamson–Hall analysis[52] (section S.3) on the XRD peaks (Figure 4b) of the as-synthesized and heated 10% TACN@Al to estimate the lattice strain on the core before and after heating. The Williamson–Hall plot presented in Figure 4c shows that the heated sample possesses a higher lattice strain ($\varepsilon = 1 \times 10^{-3}$) and crystallite size ($L = 64$ nm) compared to the unheated ($\varepsilon = 6 \times 10^{-4}$; $L = 27$ nm). The disappearance of the exothermic DSC peak (Figure 2b) associated with reaction in eq R3 in for TACN@Al implies that the heat released is possibly absorbed by simultaneous melting of Al. Although the area of the DSC exotherm underestimates the heat release associated with a gas generating reaction, in this case it is an indicator of the minimum heat delivered (~128 kJ/mol) to Al from TACN decomposition, whereas the maximum heat is limited by the calculated enthalpy of decomposition of TACN ($\Delta H = -644$ kJ/mol). Based on these two estimates, Figure 4d shows the comparison between the maximum and minimum mass percentages of Al (section S.4), the enthalpy of which can be raised to its melting point (~923 K) by the heat released from TACN. According to this estimate, a 10% TACN coating can potentially melt ~16−80 mass % of Al. As TACN forms a liquid film followed by successive gas and heat generation through reactions in eqs R2 and R3, formation of gas bubbles might lead to inhomogeneous temperature distribution across the liquid film which will result in inhomogeneous heat transfer flux across the Al/AlO_x interface, causing localized overheating
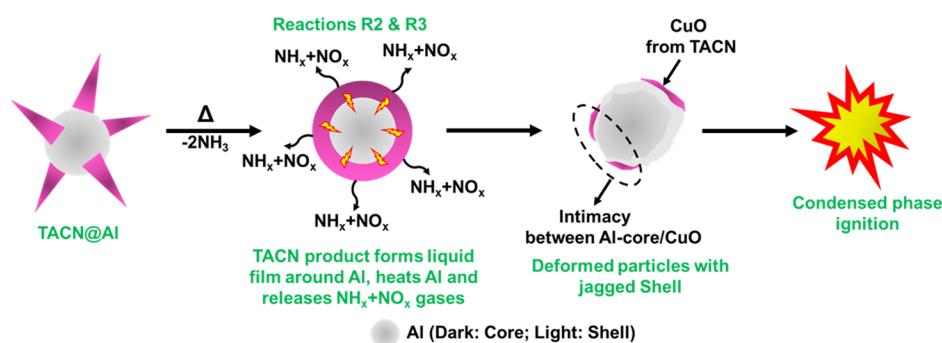
**Figure 5.** Schematic showing the overall reaction mechanism of TACN@Al nanocomposites.

and hot-spot formation.[53,54] Such localized hot spots might lead to partial melting of Al, and the expansion associated with the melting process causes molten Al to flow out of the imperfections in the shell inducing nonuniformity in the shell thickness, creating the jagged shape.[28,33,34] The inhomogeneous melting might explain the increase in the strain and the crystallite size of the core.[30,55] The nonuniformity in the thickness of the shell may also be enhanced by the localized swelling caused by high-temperature diffusion of Al cations into the interstices of the $AlO_x$ shell.[33] Table 1 presents a comparison of the microstructural evolution mechanisms of Al nanoparticles under thermally induced stresses observed by this study to previous studies in the literature.

Overall, the heat generated during the exothermic decomposition of TACN induces strain on the Al core simultaneously, causing the surrounding $AlO_x$ shell to become rough. Because of nonuniformity in the thickness of the surrounding shell, certain regions of the Al particle surface will have a thinner shell, thereby placing the Al core closer to the CuO crystallized from TACN decomposition. A thinner diffusion barrier enables the interstitial mass transfer of Al cations across the shell, initiating a condensed phase reaction between Al and CuO, which leads to the lower ignition onset ($\sim$770 K). Additionally, previous studies[22−32] have also reported that prestressing reduces the hardness of the Al particles, causing the faster expulsion of molten Al and thereby enhancing its reactivity. In the current case, the thermomechanical shock induced stress applied by TACN decomposition should also soften the Al nanoparticles, thereby enhancing their reactivity (Figure 4b−d and Figure S5). In physically mixed PM-Al/TACN powder, the contact area for heat transfer between the Al and TACN is much lower compared to the core−shell architecture. Hence, the oxidation of Al is not lowered in the case of PM-Al/TACN as observed in section 3.2.

**3.5. Discussion on Overall Mechanism.** Figure 5 summarizes the overall reaction mechanism of TACN@Al based on the aforementioned observations and inferences. On heating of TACN@Al, 2 mol of $NH_3$ is released from the decomposition of TACN through eq R1, followed by a phase transformation of the intermediate product $Cu(NH_3)_2(NO_3)_2$. The molten $Cu(NH_3)_2(NO_3)_2$ wets the surface of the Al nanoparticles forming a liquid film. Exothermic decomposition (R3) of $Cu(NH_3)_2(NO_3)_2$ to solid CuO and $NH_x + NO_x$ gases shock-heats the Al particles over the short reaction time scale. This shock-heating leads to partial liquefaction (expansion), causing some Al to leak into the inhomogeneous shell, followed by resolidification (contraction) of the Al core, thereby causing deformation of the particles and simulta-

neously resulting in corrugations at the Al core/$AlO_x$ shell interface. Because of the corrugations, the shell has nonuniform thickness with localized thinner regions, which increases the intimacy between the Al core and the CuO crystallized from (R3). The reduced interstitial diffusion length enables the Al ions to diffuse to the surface CuO, thereby initiating the condensed phase reaction and ignition process. Thus, heat generated from TACN decomposition causes in-situ stressing of Al nanoparticles which leads to their condensed phase ignition.

However, in the case of the physically mixed sample (PM-Al/TACN), the molten $Cu(NH_3)_2(NO_3)_2$ is unable to completely wet the surface of the Al nanoparticles, thereby reducing the heat transfer area. Therefore, the oxidation onset of Al in PM-Al/TACN is not lowered, and the decomposition of TACN and oxidation of Al occur separately (section 3.2). Although the TACN@Al composites are fuel-lean, the in-situ stress induction and the condensed phase ignition process will shorten the time scale of the extraction of oxidative energy from the Al core in the presence of adequate amount of oxygen sources. The higher reactivity of the TACN@Al in air and with CuO observed in ignition and combustion cell measurements also confirms the same. For the purpose of qualitative visual depiction of the decomposition and ignition process, optical snapshots of flash-heated TACN powder decomposition and 10% TACN@Al ignition captured by using a high-speed camera have been presented in Figures S8 and S9. Figure S8 clearly shows the melting of bare TACN powder (R2) forming a liquid droplet, which bubbles and releases gaseous fumes ($NH_x + NO_x$), indicating the occurrence of reactions in eqs R2 and R3. Figure S9 confirms that the fumes are released ahead of the ignition process. These images also qualitatively support the above-mentioned mechanisms.

## 4. CONCLUSIONS

In this study we show that despite having the same fuel and oxidizer combination, tetraamine copper nitrate complex (TACN)-coated Al nanocomposites (TACN@Al) synthesized by a heterogeneous crystallization method demonstrate unexpectedly lower ignition onset (by $\sim$200 K) and higher reactivity ($\sim$10×) compared to benchmark nanothermite mixture of Al/CuO. T-jump TOFMS reveals that TACN@Al releases $NO_x$ gases on decomposition of TACN at an $\sim$300 K lower temperature than their ignition temperature. Hence, the released $NO_x$ cannot initiate the ignition process acting as an oxidizer for Al. However, through TEM and XRD analysis, we show that the heat released on TACN decomposition shock-heats the Al particles, thereby enhancing the strain on the Al core, successively deforming the particles, and inducing

nonuniformity in the thickness of their inherent oxide shell. The thinner regions of the jagged oxide shell with nonuniform thickness reduce the mass transfer barrier of Al ions, enabling them to diffuse across the shell and initiate a condensed phase reaction with the CuO crystallized as a product of TACN decomposition, thereby lowering the ignition onset. These effects were not observed during the reaction of physically mixed nano-Al/micrometer TACN powder, as in that case the decomposition of TACN and oxidation of Al occurred independently because of the smaller contact area for heat transfer between TACN and Al. Hence, the thermomechanical shock provided to the Al nanoparticles on TACN decomposition plays major role in enhancing the reactivity of TACN@Al nanocomposites.

## ASSOCIATED CONTENT

### Ⓢ Supporting Information

The Supporting Information is available free of charge at https://pubs.acs.org/doi/10.1021/acsami.2c05412.

Active content of complex from TGA; SEM size distribution; T-jump TOFMS summed spectra of all samples; T-jump ignition snapshots of all samples; combustion cell measurements of all samples; T-jump TOFMS $O_2$ release profile of CuO; T-jump ignition of Al/CuO and annealed (high heating rate) Al/CuO; Williamson−Hall analysis; calculation regarding Figure 4d; visual depiction of TACN decomposition (melting and gas generation) and TACN@Al ignition process (ignition followed by gas generation) captured by a high-speed camera (PDF)

## AUTHOR INFORMATION

### Corresponding Author

Michael R. Zachariah − *Department of Chemical and Environmental Engineering, University of California, Riverside, Riverside, California 92521, United States;* ⓞ orcid.org/0000-0002-4115-3324; Email: mrz@engr.ucr.edu

### Authors

Prithwish Biswas − *Department of Chemical and Environmental Engineering, University of California, Riverside, Riverside, California 92521, United States;* ⓞ orcid.org/0000-0002-9921-2905

Feiyu Xu − *Department of Chemical and Environmental Engineering, University of California, Riverside, Riverside, California 92521, United States; Department of Chemistry and Biochemistry, University of Maryland, College Park, Maryland 20742, United States;* ⓞ orcid.org/0000-0003-0671-3485

Pankaj Ghildiyal − *Department of Chemical and Environmental Engineering, University of California, Riverside, Riverside, California 92521, United States; Department of Chemistry and Biochemistry, University of Maryland, College Park, Maryland 20742, United States;* ⓞ orcid.org/0000-0002-4422-3068

Complete contact information is available at:
https://pubs.acs.org/10.1021/acsami.2c05412

### Notes

The authors declare no competing financial interest.

## REFERENCES

(1) Hastings, D.; Rodriguez, N.; McCann, H.; Schoenitz, M.; Dreizin, E. L. Titanium-Boron Reactive Composite Powders with Variable Morphology Prepared by Arrested Reactive Milling. *Fuel* **2022**, *310*, 122313.

(2) Xu, F.; Nava, G.; Biswas, P.; Dulalia, I.; Wang, H.; Alibay, Z.; Gale, M.; Kline, D. J.; Wagner, B.; Mangolini, L.; et al. Energetic Characteristics of Hydrogenated Amorphous Silicon Nanoparticles. *Chem. Eng. J.* **2022**, *430*, 133140.

(3) Biswas, P.; Ghildiyal, P.; Kwon, H.; Wang, H.; Alibay, Z.; Xu, F.; Wang, Y.; Wong, B. M.; Zachariah, M. R. Rerouting Pathways of Solid-State Ammonia Borane Energy Release. *J. Phys. Chem. C* **2022**, *126*, 48−57.

(4) Trunov, M. A.; Schoenitz, M.; Zhu, X.; Dreizin, E. L. Effect of Polymorphic Phase Transformations in $Al_2O_3$ Film on Oxidation Kinetics of Aluminum Powders. *Combust. Flame* **2005**, *140*, 310−318.

(5) Trunov, M. A.; Umbrajkar, S. M.; Schoenitz, M.; Mang, J. T.; Dreizin, E. L. Oxidation and Melting of Aluminum Nanopowders. *J. Phys. Chem. B* **2006**, *110*, 13094−13099.

(6) Senyurt, E. I.; Dreizin, E. L. At What Ambient Temperature Can Thermal Runaway of a Burning Metal Particle Occur? *Combust. Flame* **2022**, *236*, 111800.

(7) Mursalat, M.; Huang, C.; Julien, B.; Schoenitz, M.; Esteve, A.; Rossi, C.; Dreizin, E. L. Low-Temperature Exothermic Reactions in Al/CuO Nanothermites Producing Copper Nanodots and Accelerating Combustion. *ACS Appl. Nano Mater.* **2021**, *4*, 3811−3820.

(8) Hastings, D.; Schoenitz, M.; Dreizin, E. L. Highly Reactive Spheroidal Milled Aluminum. *Materialia* **2021**, *15*, 100959.

(9) Henz, B. J.; Hawa, T.; Zachariah, M. R. On the Role of Built-in Electric Fields on the Ignition of Oxide Coated Nanoaluminum: Ion Mobility versus Fickian Diffusion. *J. Appl. Phys.* **2010**, *107*, 024901.

(10) Jiang, Y.; Deng, S.; Hong, S.; Zhao, J.; Huang, S.; Wu, C. C.; Gottfried, J. L.; Nomura, K. I.; Li, Y.; Tiwari, S.; et al. Energetic Performance of Optically Activated Aluminum/Graphene Oxide Composites. *ACS Nano* **2018**, *12*, 11366−11375.

(11) Jiang, Y.; Deng, S.; Hong, S.; Tiwari, S.; Chen, H.; Nomura, K. I.; Kalia, R. K.; Nakano, A.; Vashishta, P.; Zachariah, M. R.; et al. Synergistically Chemical and Thermal Coupling between Graphene Oxide and Graphene Fluoride for Enhancing Aluminum Combustion. *ACS Appl. Mater. Interfaces* **2020**, *12*, 7451−7458.

(12) Séverac, F.; Alphonse, P.; Estève, A.; Bancaud, A.; Rossi, C. High-Energy Al/CuO Nanocomposites Obtained by DNA-Directed Assembly. *Adv. Funct. Mater.* **2012**, *22*, 323−329.

(13) Wang, X.; Zhou, W.; Delisio, J. B.; Egan, G. C.; Zachariah, M. R. Doped δ-Bismuth Oxides to Investigate Oxygen Ion Transport as a Metric for Condensed Phase Thermite Ignition. *Phys. Chem. Chem. Phys.* **2017**, *19*, 12749−12758.

(14) Wang, X.; Wu, T.; Zachariah, M. R. Doped Perovskites to Evaluate the Relationship between Fuel-Oxidizer Thermite Ignition and Bond Energy, Electronegativity, and Oxygen Vacancy. *J. Phys. Chem. C* **2017**, *121*, 147−152.

(15) Xu, F.; Hirt, B.; Biswas, P.; Kline, D. J.; Yang, Y.; Wang, H.; Sehirlioglu, A.; Zachariah, M. R. Superior Reactivity of Ferroelectric Bi2WO6/Aluminum Metastable Intermolecular Composite. *Chem. Eng. Sci.* **2022**, *247*, 116898.

(16) Chen, Y.; Ren, W.; Zheng, Z.; Wu, G.; Hu, B.; Chen, J.; Wang, J.; Yu, C.; Ma, K.; Zhou, X.; et al. Reactivity Adjustment from the

Contact Extent between CuO and Al Phases in Nanothermites. *Chem. Eng. J.* **2020**, *402*, 126288.

(17) Wang, H.; Kline, D. J.; Biswas, P.; Zachariah, M. R. Connecting Agglomeration and Burn Rate in a Thermite Reaction: Role of Oxidizer Morphology. *Combust. Flame* **2021**, *231*, 111492.

(18) Wang, W.; Li, H.; Zhang, M.; Zhao, F.; Xu, S.; Wang, C.; Qin, Z.; An, T.; Xu, K. Effects of Oxidizer and Architecture on the Thermochemical Reactivity, Laser Ignition and Combustion Properties of Nanothermite. *Fuel* **2022**, *314*, 123141.

(19) Xu, F.; Biswas, P.; Nava, G.; Schwan, J.; Kline, D. J.; Rehwoldt, M. C.; Mangolini, L.; Zachariah, M. R. Tuning the Reactivity and Energy Release Rate of I2O5 Based Ternary Thermite Systems. *Combust. Flame* **2021**, *228*, 210−217.

(20) Ghildiyal, P.; Ke, X.; Biswas, P.; Nava, G.; Schwan, J.; Xu, F.; Kline, D. J.; Wang, H.; Mangolini, L.; et al. Silicon Nanoparticles for the Reactivity and Energetic Density Enhancement of Energetic-Biocidal Mesoparticle Composites. *ACS Appl. Mater. Interfaces* **2021**, *13*, 458−467.

(21) Zhu, Y.; Zhou, X.; Xu, J.; Ma, X.; Ye, Y.; Yang, G.; Zhang, K. In Situ Preparation of Explosive Embedded CuO/Al/CL20 Nano-energetic Composite with Enhanced Reactivity. *Chem. Eng. J.* **2018**, *354*, 885−895.

(22) Hill, K. J.; Pantoya, M. L.; Washburn, E.; Kalman, J. Single Particle Combustion of Pre-Stressed Aluminum. *Materials* **2019**, *12*, 1737.

(23) Hill, K. J.; Warzywoda, J.; Pantoya, M. L.; Levitas, V. I. Dropping the Hammer: Examining Impact Ignition and Combustion Using Pre-Stressed Aluminum Powder. *J. Appl. Phys.* **2017**, *122*, 125102.

(24) Hill, K. J.; Tamura, N.; Levitas, V. I.; Pantoya, M. L. Impact Ignition and Combustion of Micron-Scale Aluminum Particles Pre-Stressed with Different Quenching Rates. *J. Appl. Phys.* **2018**, *124*, 115903.

(25) Williams, A.; Shancita, I.; Vaz, N. G.; Tran-Ngo, T.; Demko, A.; Altman, I.; Hill, K. J.; Tunega, D.; Aquino, A. J. A.; Pantoya, M. L. Stress-Altered Aluminum Powder Dust Combustion. *J. Appl. Phys.* **2020**, *127*, 175110.

(26) Altman, I.; Demko, A.; Hill, K.; Pantoya, M. On the Possible Coexistence of Two Different Regimes of Metal Particle Combustion. *Combust. Flame* **2020**, *221*, 416−419.

(27) Bello, M. N.; Williams, A. M.; Levitas, V. I.; Tamura, N.; Unruh, D. K.; Warzywoda, J.; Pantoya, M. L. Highly Reactive Energetic Films by Pre-Stressing Nano-Aluminum Particles. *RSC Adv.* **2019**, *9*, 40607−40617.

(28) Jacob, R. J.; Hill, K. J.; Yang, Y.; Pantoya, M. L.; Zachariah, M. R. Pre-Stressing Aluminum Nanoparticles as a Strategy to Enhance Reactivity of Nanothermite Composites. *Combust. Flame* **2019**, *205*, 33−40.

(29) Bello, M. N.; Williams, A.; Shancita, I.; Hoque, M. N.; Christopher, G.; Aquino, A. J. A.; Tunega, D.; Pantoya, M. L. Synthesis and Characterization of Polymeric Films with Stress-Altered Aluminum Particle Fillers. *J. Mater. Sci.* **2020**, *55*, 14229−14242.

(30) McCollum, J.; Smith, D. K.; Hill, K. J.; Pantoya, M. L.; Warzywoda, J.; Tamura, N. A Slice of an Aluminum Particle: Examining Grains, Strain and Reactivity. *Combust. Flame* **2016**, *173*, 229−234.

(31) Lucas, M.; Brotton, S. J.; Min, A.; Woodruff, C.; Pantoya, M. L.; Kaiser, R. I. Effects of Size and Prestressing of Aluminum Particles on the Oxidation of Levitated Exo-Tetrahydrodicyclopentadiene Droplets. *J. Phys. Chem. A* **2020**, *124*, 1489−1507.

(32) Dikici, B.; Pantoya, M. L.; Levitas, V. The Effect of Pre-Heating on Flame Propagation in Nanocomposite Thermites. *Combust. Flame* **2010**, *157*, 1581−1585.

(33) Firmansyah, D. A.; Sullivan, K.; Lee, K. S.; Kim, Y. H.; Zahaf, R.; Zachariah, M. R.; Lee, D. Microstructural Behavior of the Alumina Shell and Aluminum Core before and after Melting of Aluminum Nanoparticles. *J. Phys. Chem. C* **2012**, *116*, 404−411.

(34) Wu, T.; Lahiner, G.; Tenailleau, C.; Reig, B.; Hungria, T.; Esteve, A.; Rossi, C. Unexpected Enhanced Reactivity of Aluminized

Nanothermites by Accelerated Aging. *Chem. Eng. J.* **2021**, *418*, 129432.

(35) Southern, T. M.; Wendlandt, W. W. The Thermal Decomposition of Metal Complexes—XX: Some Amine Copper(II) Nitrate Complexes. *J. Inorg. Nucl. Chem.* **1970**, *32*, 3783−3792.

(36) Mathew, S.; Nair, C. G. R.; Ninan, K. N. Thermal Decomposition Studies on Amine Complexes of Copper(II) Nitrate in Solid State. *Bull. Chem. Soc. Jpn.* **1991**, *64*, 3207−3209.

(37) Künzel, M.; Vodochodský, O.; Matyáš, R.; Jalový, Z.; Pachman, J.; Maixner, J. Tetraamminecopper(II) Nitrate and Its Effects on Ammonium Nitrate(V). *Cent. Eur. J. Energy Mater.* **2017**, *14*, 169−183.

(38) Liszka-Skoczylas, M.; Mikuli, E.; Szklarzewicz, J.; Hetmańczyk, J. Thermal Behaviour, Phase Transition and Molecular Motions in $[Co(NH_3)_6](NO_3)_2$. *Thermochim. Acta* **2009**, *496*, 38−44.

(39) Pradère, C.; Suhard, S.; Vendier, L.; Jacob, G.; Chaudret, B.; Sabo-Etienne, S. Heterometallic Werner Complexes as Energetic Materials. *Dalton T.* **2008**, 2725−2731.

(40) Sullivan, K. T.; Piekiel, N. W.; Wu, C.; Chowdhury, S.; Kelly, S. T.; Hufnagel, T. C.; Fezzaa, K.; Zachariah, M. R. Reactive Sintering: An Important Component in the Combustion of Nanocomposite Thermites. *Combust. Flame* **2012**, *159*, 2−15.

(41) Wang, H.; Kline, D. J.; Zachariah, M. R. In-Operando High-Speed Microscopy and Thermometry of Reaction Propagation and Sintering in a Nanocomposite. *Nat. Commun.* **2019**, *10*, 3032.

(42) Egan, G. C.; Lagrange, T.; Zachariah, M. R. Time-Resolved Nanosecond Imaging of Nanoscale Condensed Phase Reaction. *J. Phys. Chem. C* **2015**, *119*, 2792−2797.

(43) Brotman, S.; Rouhani, M. D.; Rossi, C.; Estève, A. A Condensed Phase Model of the Initial Al/CuO Reaction Stage to Interpret Experimental Findings. *J. Appl. Phys.* **2019**, *125*, 035102.

(44) Wang, H.; Jian, G.; Egan, G. C.; Zachariah, M. R. Assembly and Reactive Properties of Al/CuO Based Nanothermite Microparticles. *Combust. Flame* **2014**, *161*, 2203−2208.

(45) Wu, T.; Sevely, F.; Julien, B.; Sodre, F.; Cure, J.; Tenailleau, C.; Esteve, A.; Rossi, C. New Coordination Complexes-Based Gas-Generating Energetic Composites. *Combust. Flame* **2020**, *219*, 478−487.

(46) Sevely, F.; Liu, X.; Wu, T.; Mesnilgrente, F.; Franc, B.; Assie-Souleille, S.; Dollat, X.; Rossi, C. Effect of Process Parameters on the Properties of Direct Written Gas-Generating Reactive Layers. *ACS Appl. Polym. Mater.* **2021**, *3*, 3972−3980.

(47) Wu, T.; Sevely, F.; Pelloquin, S.; Assié-Souleille, S.; Estève, A.; Rossi, C. Enhanced Reactivity of Copper Complex-Based Reactive Materials via Mechanical Milling. *Combust. Flame* **2021**, *233*, 111598.

(48) Jian, G.; Zhou, L.; Piekiel, N. W.; Zachariah, M. R. Low Effective Activation Energies for Oxygen Release from Metal Oxides: Evidence for Mass-Transfer Limits at High Heating Rates. *ChemPhysChem* **2014**, *15*, 1666−1672.

(49) Rehwoldt, M. C.; Wang, Y.; Xu, F.; Ghildiyal, P.; Zachariah, M. R. High-Temperature Interactions of Metal Oxides and a PVDF Binder. *ACS Appl. Mater. Interfaces* **2022**, *14*, 8938−8946.

(50) Zhou, W.; DeLisio, J. B.; Wang, X.; Egan, G. C.; Zachariah, M. R. Evaluating Free vs Bound Oxygen on Ignition of Nano-Aluminum Based Energetics Leads to a Critical Reaction Rate Criterion. *J. Appl. Phys.* **2015**, *118*, 114303.

(51) Jian, G.; Chowdhury, S.; Sullivan, K.; Zachariah, M. R. Nanothermite Reactions: Is Gas Phase Oxygen Generation from the Oxygen Carrier an Essential Prerequisite to Ignition? *Combust. Flame* **2013**, *160*, 432−437.

(52) Kunka, C.; Boyce, B. L.; Foiles, S. M.; Dingreville, R. Revealing Inconsistencies in X-Ray Width Methods for Nanomaterials. *Nanoscale* **2019**, *11*, 22456−22466.

(53) Fedorchenko, A. I.; Hruby, J. On Formation of Dry Spots in Heated Liquid Films. *Phys. Fluids* **2021**, *33*, 023601.

(54) Tenzer, F. M.; Roisman, I. v.; Tropea, C. Fast Transient Spray Cooling of a Hot Thick Target. *J. Fluid Mech.* **2019**, *881*, 84−103.

(55) Levitas, V. I.; Samani, K. Size and Mechanics Effects in Surface-Induced Melting of Nanoparticles. *Nat. Commun.* **2011**, *2*, 284.